Sonoporation from Jetting Cavitation Bubbles

Claus-Dieter Ohl,* Manish Arora,* Roy Ikink,* Nico de Jong,*† Michel Versluis,* Michael Delius,‡ and Detlef Lohse*

*Faculty of Science and Technology, Physics of Fluids, University of Twente, Enschede, The Netherlands; †Experimental Echocardiography, Thoraxcentre, Erasmus Medisch Centrum, Rotterdam, The Netherlands; and ‡Institute for Surgical Research, University of Munich, Klinikum Grosshadern, Munich, Germany

ABSTRACT The fluid dynamic interaction of cavitation bubbles with adherent cells on a substrate is experimentally investigated. We find that the nonspherical collapse of bubbles near to the boundary is responsible for cell detachment. High-speed photography reveals that a wall bounded flow leads to the detachment of cells. Cells at the edge of the circular area of detachment are found to be permanently porated, whereas cells at some distance from the detachment area undergo viable cell membrane poration (sonoporation). The wall flow field leading to cell detachment is modeled with a self-similar solution for a wall jet, together with a kinetic ansatz of adhesive bond rupture. The self-similar solution for the δ-type wall jet compares very well with the full solution of the Navier-Stokes equation for a jet of finite thickness. Apart from annular sites of sonoporation we also find more homogenous patterns of molecule delivery with no cell detachment.

INTRODUCTION

Sonoporation—the rupture of cell membranes by acoustical means—might allow novel strategies to noninvasively deliver large-sized molecules into cells for therapeutic applications (1,2). Gaining a better understanding of which physical mechanisms are responsible for the rupture of the cell membranes is crucial to increase the yield of treated cells. The important finding that sonoporation (3–5) is drastically enhanced when bubbles are present during the acoustic exposure hints that a fluid dynamic interaction between the pulsating bubble and the cell is leading to membrane poration. Still, the precise mechanisms of pore opening and the uptake of exterior liquid are not determined in detail. Possible candidates are shock waves (6,7) or acoustic transients emitted from the bubble (8); extensional flow (9) straining the membrane during expansion, shrinkage, or microstreaming (10); shearing flow near no-slip boundaries (11); or a micro-jetting flow that is excited when the bubble collapses aspherically (12).

In general, it can be distinguished between two acoustic approaches to excite the bubble activity near to cells: Either with a quasi-continuous ultrasound (1) or with a single intensive wave (13). In quasi-continuous ultrasound applications, cells are exposed to many acoustic cycles. Then, bubbles have enough time to grow by rectified diffusion (14–17) from small nuclei to resonance size. In contrast, single wave excitation causes nucleation and drives the bubble to a single large volume oscillation. This can only be achieved for sufficient amplitudes of the negative pressure. For this purpose, shock wave generators, which are commonly used for the fragmentation of renal stones (shock wave lithotripsy), have proven to reach sufficient tensile stress. Other methods to generate shock waves involve the use of lasers (6,18) or shock tubes (19). In a recent experimental study, a laser-induced cavitation bubble was generated near to a substrate with adherent rat kidney cells (20). The authors concluded that the shock wave launched from the cooling plasma at the laser focus causes cell lysis and the lysis region is fully developed within 1 μs after the laser pulse.

Here, we show that cavitation bubbles cause membrane poration to cells plated on a substrate through a rather complex sequence of events: Bubbles become nucleated and expand explosively. During the collapse of bubbles near to the substrate, a jetting flow toward the substrate is excited. When this jet flow impacts onto the boundary, it spreads out radially along the substrate. It is this flow which—together with the no-slip velocity boundary condition at the wall covered with cells—causes a strong gradient in the velocity component parallel with the substrate. The resulting shear stress acts on the cells attached to the boundary.

In this article we will first present a picture covering a large area of cells treated with a single shock wave. Next, fluorescence and electron micrographs distinguish locations of permanent and viable sonoporation. Then the dynamics of bubble-cell interaction is revealed with high-speed photography. These observations are compared to a simple model of wall-flow caused by the collapsing bubble. This simple model reasonably agrees with the data. Note that we do not present a full theoretical or numerical description of the wall jet here. (Such a description has been done by Blake and coworkers; see, e.g., (28,31,38,39,41).)

EXPERIMENTAL METHODS

Shock wave generation and high-speed imaging

The experimental setup, depicted in Fig. 1, consists of the shock wave source, a 35 mm polystyrene petri dish (Fisher, 's Hertogenbosch, Netherlands)

Submitted September 30, 2005, and accepted for publication August 18, 2006.

Address reprint requests to Dr. Claus-Dieter Ohl, Tel.: 31-53-489-5604; E-mail: c.d.ohl@tnw.utwente.nl.

0006-3495/06/12/4285/11 $2.00

doi: 10.1529/biophysj.105.075366

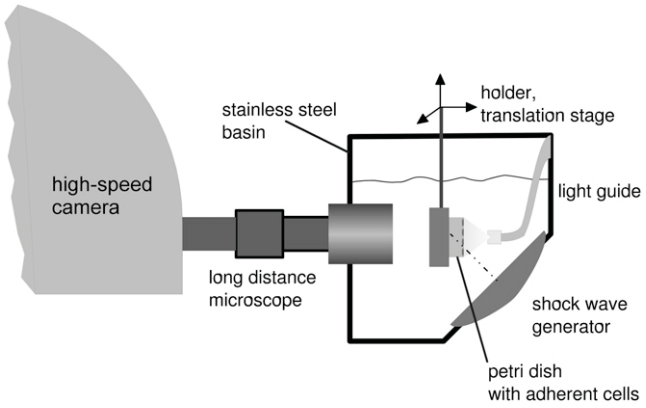

FIGURE 1 Sketch of the experimental setup. Shock waves in the water basin are generated with a piezoelectric transducer and are focused under an angle of 45° to the horizontal. The adhering HeLa cells on the petri dish are facing the shock-wave generator and are illuminated with a light guide. Imaging of the cell layer is done with a long-working-distance microscope connected to the high-speed framing system Brandaris 128.

with adherent cells on the substrate facing the transducer, the imaging and illumination devices, and digital delay lines. A single finite amplitude wave is generated with a focused piezoelectric source; it is a slightly modified commercial extracorporeal lithotripter Piezolith 3000 (Richard Wolf, Knittlingen, Germany). The diameter of the shock wave source is 251 mm and the focusing angle 94°. In the experiments presented here, only the frontal of the two piezoelectric layers is operated at a moderately low amplitude of 5 kV. The duration of the tensile wave is 2.5 μs and reaches an amplitude of -4 MPa. The acoustic axis of the source is at an angle of 45° to the horizontal plane. The transducer is located at the bottom of a stainless steel container having glass windows on all three sides. The container is filled with filtered, deionized, and degassed water (O_2 concentration 3.3 mg/l of water) at room temperature. The temperature of the lithotripter bath and the cell medium is ~22°C.

Recordings are taken with a rotating mirror camera, Brandaris 128 (21), at a frame rate of $\sim 250 \times 10^3$ frames per second. It is equipped with 128 individual charge-coupled device cameras that are read out digitally. The size of each frame is 500 × 292 pixels. Illumination is provided with a continuous lamp connected to a flexible light guide, which is submerged in the water and positioned close to the flask. A long distance microscope (model No. K2, Infinity, Stuttgart, Germany) with a CF-3 objective (120 mm working distance in air) images the scene. A field lens at the primary image plane of the high-speed camera collects the illumination light (Köhler-type illumination).

Cell assay and viability checks

Cervix cancer cells (HeLa) were grown at 37°C and 5% CO_2 in Iscove's modified Dulbecco's medium (Invitrogen, Breda, Netherlands) supplemented with 10% fetal bovine serum (Invitrogen) until they form a nearly confluent monolayer. The medium was enriched with a solution of antibiotics and antimycotic (No. 15240-062, Gibco, Big Cabin, OK) with 100 units/ml penicillin, 100 μg/ml streptomycin, and 0.25 μg/ml amphotericin B. The cell density in the flask at the time of use was ~500 cells/mm^2. The cells were grown in 35-mm diameter petri dishes. Before the exposure with shock waves, the petri dishes were attached to a holder with an imaging window and filled completely with medium and 1 mg/ml of the cell impermeant fluorophore Calcein (Merck, Darmstadt, Germany). Special threads into the petri dish holder allowed filling and its closure such that no air bubbles become trapped within. Then the holder was attached to a three-axis translation stage and positioned at the focus of the sound field. Cell viability was tested by adding ethidium bromide (Fluka, Zwijndrecht, Netherlands) after shock wave exposure. By staining the cell culture at a final concentrations of 5 μg/ml, ruptured cells appear red due to the intercalation of ethidium bromide into their DNA.

Scanning electron microscopy and cell preparation

Cells after exposure to the shock wave and washing were fixed with a 5% glutaraldehyde solution in PBS for 30 min. Dehydration was carried out in graded series of ethanol (50%, 70%, 90%, 95%, and 100% for 20 min each). Then the medium for the dehydrated cells was replaced by 50% mixture of tetramethylsilane and ethanol (22). Finally, cells were immersed in 100% tetramethylsilane for 10 min and air-dried at room temperature. All the specimens were mounted on metal stubs with carbon-conducting tape and were observed with a low-voltage scanning electron microscope (Gemini 1550 FEG, Leo Elektronenmikroskopie, Oberkochen, Germany) at voltages between 0.5 kV and 1.2 kV. Due to the low voltage operation mode it was not necessary to deposit a conducting metal layer onto the specimen.

Large-scale fluorescence microscopy

After the application of a single shock wave, molecular uptake is scattered over an area of typically >1 cm^2. Simple imaging of the complete pattern using a camera connected to the microscope is not feasible without the loss of the details on the size of individual cells. Therefore, we applied a digital image processing procedure named ''image stitching,'' where multiple partly overlapping images of the substrate are taken. After suitable image processing steps to equalize the image brightness of the individual images, these are then combined into a single large-scale picture.

RESULTS AND DISCUSSION

Large-scale spatial distribution of molecular uptake

Fig. 2 *b* demonstrates the spatial pattern of molecular uptake after a single shock-wave exposure. The image is constructed from multiple stitched images covering an area of 9 × 22.4 mm^2. The fluorescence picture is converted into grayscales, where brighter pixels indicate drug uptake. Three partially overlapping regions are nicely distinguishable in Fig. 2. In region *A*, we find most prominent circular patterns. There, mainly isolated bubbles collapse and detach disk-shaped areas surrounded by an annular pattern of calcein uptake. Similar patterns of uptake are found in region *C*, but far fewer rings are found here. In contrast, region *B* being between regions *A* and *C* shows a more homogeneous pattern of drug delivery spreading diffusively over an area of ~4 × 4 mm^2.

We can correlate these regions with the bubble clusters generated within the flask as sketched in Fig. 2 *a* (for details, see (23,24)). The incoming wave creates a bubble cluster with its major axis inclined under 45° to the front surface of the petri dish. Some portion of the pressure wave (~30%) is reflected at the back surface of the petri dish, and a second bubble cluster separated in space from the primary one is formed. Thus, near-surface bubble collapse takes place at two separate areas on the petri dish, regions *A* and *C*.

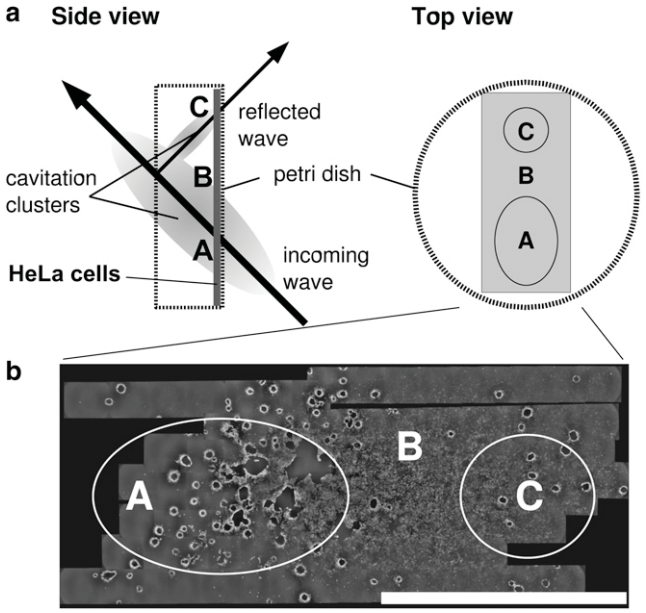

FIGURE 2 (*a*) Sketch of the side view and top view of the bubble cluster. The incoming wave enters under an angle of 45°. Two bubble clusters are generated; one from the main wave, and a smaller one from the reflection at the inner surface of the petri dish. The side view (*right*) depicts areas *A* and *C* where bubble-collapse onto the adherent cells takes place. Area *B* is largely free of bubbles. (*b*) Large-scale fluorescence microscope picture of the substrate after the bubble collapse. Annular structures of molecular uptake (*bright cells*) are found in regions *A* and *C*, where region *B* is covered with a diffuse pattern. The white bar denotes a scale of 10 mm.

Region *B* is practically free of bubbles, although we find molecular uptake at lower intensity levels of the fluorescence emission. This region is closest to the center of the bubble cluster generated within the petri dish. The collective collapse of this cluster acts like a sink flow drawing fluid toward its center. We speculate that it might be the shear flow generated by the violent cluster collapse that causes the drug uptake in region *B*. This hypothesis would explain that the homogeneous and diffuse pattern is only observed between regions *A* and *C* being nearest to the center of the main cavitation cluster.

Closeups of detachment sites

Two closeups with an additional viability staining from region *A* are depicted in Fig. 3. There, ethidium-bromide is used to stain permanently porated cells red and viable calcein uptake is indicated with green fluorescence. In general, we find disk-shaped detachment sites with diameters of the order of the maximum bubble diameter. The central cleared areas are bordered with an inner annular ring of killed cells. A typical example is given in the left portion of Fig. 3. There, the area of cell killing (*red-stained cells*) has a width of ~5 cell diameters wide. These cells will eventually round-up due to their loss of adhesion ability. In contrast, the cells in the outer annular structure (*stained green*) stay adhesive.

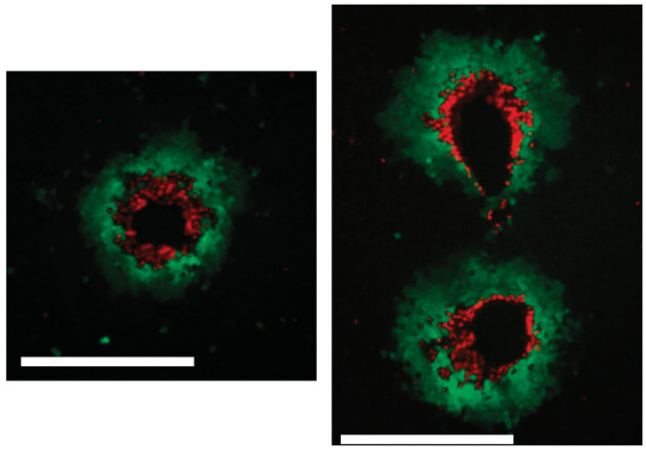

FIGURE 3 Closeup of typical cell detachment areas found in region *A* of Fig. 2. Viable porated cells are colored green (calcein uptake) and red cells are stained with ethidium bromide (permanent poration). The left image depicts the detachment and sonoporation from a single bubble, and the right image depicts two bubbles that have collapsed close to each other. The bar denotes 0.5 mm.

We find when regions of detachment are close to each other that the circular shape is disturbed. An interesting pattern of molecular delivery is depicted in Fig. 3, right. The upper cleared area possesses an egg shape, which narrows toward the lower site of detachment. A plausible scenario causing this pattern might be a translational movement of the bubbles toward each other during the collapse dynamics. Bubbles collapsing in phase are accelerated toward each other (see, e.g., (25)). Thereby, the jet flow will not impact perpendicular toward the substrate but under some angle. The inclined jet flow might be responsible for the cusp shape area of detachment observed in the upper site of drug delivery. In contrast, more isolated areas of detachment (i.e., lower bubble density) depict a more circular area of detachment, which suggests that bubble-bubble interaction plays a role in sonoporation.

As pointed out above, region *B*, Fig. 2, shows a much different uptake pattern. A closeup from region *B* with ethidium-bromide staining is depicted in Fig. 4. We find a homogeneous delivery pattern with ~15% of the cells showing permanent poration (*colored red*). This observation can be explained with a flow generated at a larger scale from the collapsing cloud above the substrate. It will resemble to some extent the flow from a large bubble collapsing at some distance from the substrate. The area where cells are subjected to highest shear rates from this flow pattern will be the one closest to the center of the cloud. From geometrical considerations, this area is located between regions *A* and region *C* in Fig. 2.

Cell membrane morphology

Scanning electron microscopy (SEM) reveals changes on much smaller scales as compared to fluorescence light-microscopy.

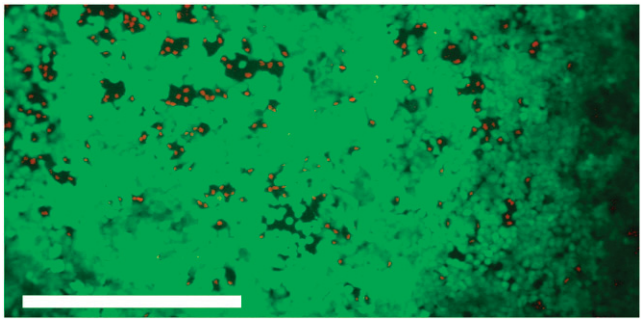

FIGURE 4 Closeup of typical cell detachment areas found in region *B* of Fig. 2. Viable porated cells are colored green (calcein uptake) and red cells are stained with ethidium bromide (permanent poration). Approximately 15% of the cells are permanently porated. The bar denotes 0.5 mm.

Here, we apply SEM to study the morphological structure of the cell membrane after the exposure to cavitation bubbles. Fig. 5 depicts with increasing magnification cells at the borderline between the area of detachment and attachment. The leftmost frame in Fig. 5 shows a typical disk-shaped area where single cavitation bubble collapse has taken place. By increasing the magnification (Fig. 5 *b*), it is revealed that the cells at the boundary have rounded up, whereas some cell-diameter away, cells are unaffected and still have a flat shape. In addition, cells at the boundary have piled up. At the highest magnification (Fig. 5 *c*), structural damage indicated with arrows of some of the rounded-up cells becomes evident. The shape and size of the lesions points to ruptured adhesion sites with cytoskeleton attachment. The piling up of the damaged cells can be explained that these cells have lost not all of their junctions but remain partially connected to neighboring cells. Thus, the flow has transported them on top of the cells while remaining partly attached.

The diameter of the pores is $\sim 1\ \mu$m. Most probably their large size prevented a closure between shock-wave exposure and fixation with glutaraldehyde, which was conducted $\sim$5 min after shock-wave exposure. In contrast, smaller and repairable pores close earlier (26). This explains why viable porated cells and ''untreated'' cells far away from detachment areas look essentially the same.

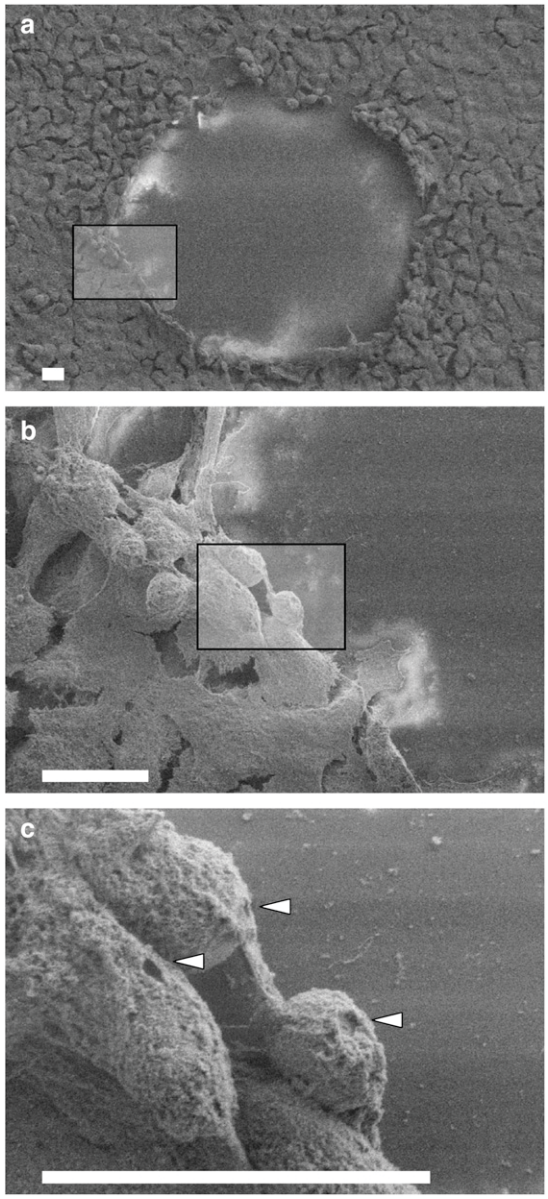

FIGURE 5 Three scanning electron microscopy (SEM) micrographs with increasing magnification from left to right. The white bar denotes a length of 20 μm. (*a*) Overview of a disk-shaped detachment site. (*b*) Magnified view of the grayed area in *a* showing rounded and piled-up cells at the border and flat cells further away. (*c*) The rounded cells at the border reveal structural damage on their membrane indicated with white arrows.

Cavitation-induced detachment dynamics

Fig. 6 depicts selected frames taken from a recording with the framing camera Brandaris 128 (21) at 230,000 frames per second. The numbers in the upper right display the time passed from the start of the negative pressure wave in microseconds. The recording is taken perpendicular to the substrate. Thus the dynamics is seen in a top view looking on the blurry layer of cells. Two stages of the dynamics can be distinguished, namely, the bubble oscillation and the process of cell detachment.

At first, a mainly isolated bubble expands, reaches maximum size, and collapses at $\sim t \approx 154\ \mu$s. The time to collapse an empty, spherical, isolated bubble of radius $R_{\max}$ to zero size is given by the Rayleigh collapse time $0.9R_{\max}\sqrt{\rho/P_0}$, where ρ and P_0 in Eq. 1 are the density of the liquid and the pressure far from the bubble, respectively. As here the bubble is not isolated but close to a wall, we allow for a prolongation factor α, which depends on the distance of the bubble center from the rigid boundary and is of order 1 (27,28). The collapse time then is

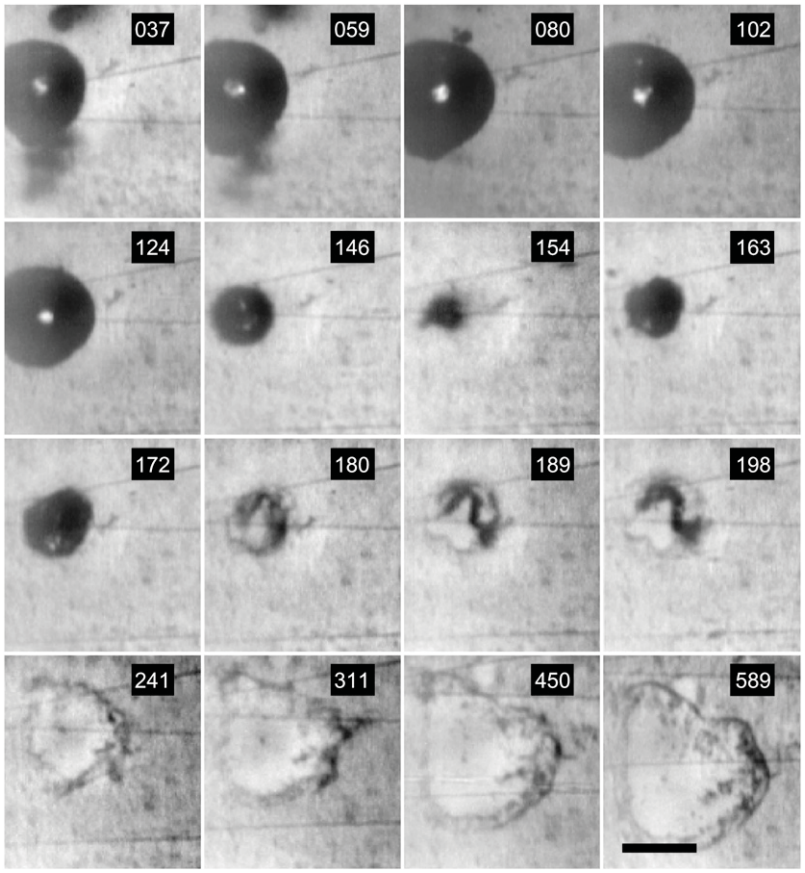

FIGURE 6 Detachment dynamics caused by the collapse of a single bubble close to a layer of adherent cells (shaded background). Here, selected frames from a framing sequence taken at 230,000 frames per second are depicted. The solid bar in the last frame denotes a scale of 1 mm. The numbers in the upper right of the frames indicate the elapsed time in microseconds after the start of the negative pressure. The bubble reaches maximum size at $\sim t = 80$ μs and shrinks to its smallest size at $t = 154$ μs. Then it reexpands as a corrugated toroidal bubble. From time $t = 180$ μs, the rim of the detached area becomes visible. The area continuous to expand even after the bubble has disintegrated.

$$T_c \approx \alpha 0.9 R_{max} \sqrt{\frac{\rho}{P_0}}. \quad (1)$$

For $\alpha = 1$, the measured collapse time of $T_C = 77$ μs would correspond to a maximum bubble size of $R_{max} \approx 0.85$ mm. However, the presence of the boundary increases the collapse time, i.e., $\alpha > 1$ in Eq. 1. Therefore, the maximum bubble radius is slightly overestimated when taking $\alpha = 1$. Indeed, the measured radius is slightly smaller, namely 0.8 mm. The assumption of a Rayleigh collapse time holds only for a bubble driven by a constant (ambient) pressure. This condition is fulfilled in this experiment because the duration of the tensile wave is only a few microseconds and therefore negligible compared to duration of the first oscillation cycle.

The bubble rebounces after the first collapse as a toroid with a corrugated surface. This toroidal structure results from the liquid jet flow toward the substrate. After the rebounce, a second much weaker volume oscillation is observed before the bubble finally disintegrates at $t \approx 200$ μs.

The second dynamical stage in Fig. 6 is the growth of the cell-depleted area first visible at ~ 180 μs. Initially, the central cleared area is surrounded by the remains of the toroidal bubble. The initial size of the depleted area is comparable with the size of the toroidal bubble. In the beginning, the depleted area grows at a radial velocity of 2 m/s. Later it decreases within the captured sequence to 0.4 m/s. Interestingly, no cell removal is observed during the early phase of the bubble collapse.

Fig. 7 depicts the temporal evolution of the bubble radius and the equivalent radius of the area cleared from cells. The cleared area approaches an averaged radius of 0.95 mm asymptotically. The most remarkable and important experimental finding is that, although the bubble has already disintegrated, the growth of the cell depletion area still continues.

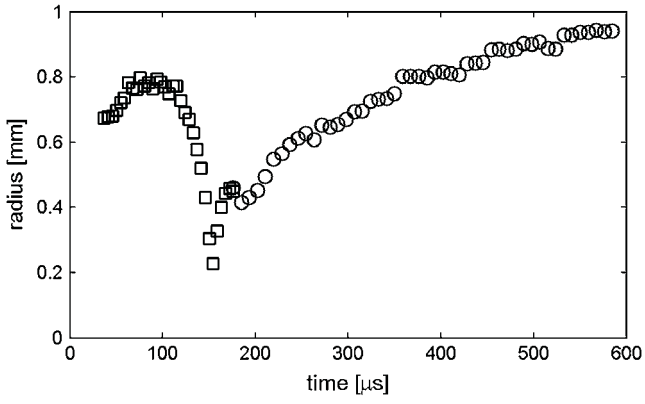

FIGURE 7 Radius of the bubble (□) and the size of the detached area (○) as a function of time. Zero time denotes the instant when the negative pressure wave reaches the cells.

A similar pattern of cell removal has been observed by Vogel et al. (29) after cavitation bubble dynamics at the corneal endothelium. In this reference it has been argued that the ''denudation of Descemet's membrane. . .is probably caused by the jet flow on the corneal surface directed radially outward from the impact site.'' This speculation is consistent with our observations.

Simple model for the shear flow

We now estimate the size of the lesions observed on the substrate as a function of the maximum bubble radius.

As already mentioned, a bubble that collapses near to a boundary develops a jet flow through the center of the bubble. The jet flow eventually pinches the bubble wall toward the rigid boundary. In general, the jet flow develops during the shrinkage of the bubble, and the maximum velocity of the jet tip strongly depends on the standoff distance of the bubble center from the boundary. We expect that not the maximum jet wall velocity but the averaged jet velocity is of greater importance. This is supported by the observation that the detachment of the cells occurs on a long timescale (on the order of the bubble collapse time). In contrast, the maximum jet velocity is only reached for a short duration around the final stage of bubble collapse (30,31). In an experimental study (32) the jet impact velocities from relatively large bubbles ($R_{\max} = 1.45$ mm) were measured. Values increasing from 5 m/s to 80 m/s (for shorter distances to the boundary) were obtained.

The interaction of a nonstationary jet flow with the adherent cells is very complex. Therefore, in a simplified model we assume that the jet impinges with a constant (i.e., stationary) flow velocity on the substrate. This flow velocity is identified with the averaged jet velocity. Unfortunately, no experimental data on the time-averaged velocity is available in literature. Therefore, a lower bound of the averaged impact jet velocity u_{jet} is estimated under the assumption that the jet flow develops during the shrinkage of the bubble from its maximum radius, $R_{\max}$. The impact of the jet occurs before the bubble reaches minimum size, and the jet flow dies out during the reexpansion of the bubble. An approximate timescale for the jet flow duration is the Rayleigh collapse time T_c (see Eq. 1). Thus, the averaged jet velocity is estimated as

$$u_{\text{jet}} = 2R_{\max}/T_c \approx \frac{2}{\alpha}\sqrt{\frac{P_0}{\rho}}. \tag{2}$$

Interestingly, the averaged jet velocity is independent of the bubble size. In literature, up to now the focus was on maximal velocities. Equation 2 is an interesting prediction that should be checked in boundary integral simulations.

Let us define a jet-based Reynolds number

$$Re = \frac{2r_{\text{jet}}u_{\text{jet}}}{\nu}, \tag{3}$$

where r_{jet} is the radius of the jet, and ν the kinematic viscosity of the liquid. Experiments (33) suggest that the jet radius scales approximately with 1/10th of the bubble radius. This allows us to write Re in terms of the bubble radius:

$$Re \approx \frac{1}{5}\frac{R_{\max}u_{\text{jet}}}{\nu} \approx 2R_{\max}[1/\mu\text{m}]. \tag{4}$$

The last expression in Eq. 4 is approximately valid for a bubble in water at ambient atmospheric pressure.

To get an idea of the flow, we will address the flow field induced from the jet only. Therefore, we neglect the flow field generated from the collapsing bubble. This serious simplification is examined in the Appendix. Further, as a limiting case we assume a stationary flow impacting vertically on the surface. The aim of this exercise is to get an idea of the strength of the shear stress at the wall.

In this limiting case, the flow is called ''Glauert's wall jet'' (34). Glauert obtained this solution through a similarity analysis. In his derivation and analytical solution of the boundary layer equation he had to neglect the region around the stagnation point (i.e., near to the point of impact). Therefore, we compare in a second step his solution with a full numerical solution to estimate the range of validity of the Glauert solution.

Glauert's similarity solution for the horizontal velocity u, the vertical velocity v, and the wall shear stress τ can be written in terms of the similarity variable $\eta = (135F/(32\nu^3x^5))^{1/4}y$ (the reduced wall distance) with $F = 3\nu^4/(40u_{\text{jet}})$. It reads

$$u = \left(\frac{15F}{2\nu x^3}\right)^{1/2}\frac{df(\eta)}{d\eta}, \tag{5}$$

$$v = \frac{15}{16}y\left(\frac{40F}{3x^5}\right)^{1/2}\frac{df(\eta)}{d\eta} - \frac{3}{4}\left(\frac{40F\nu}{3x^5}\right)^{1/4}f(\eta), \tag{6}$$

$$\tau = \rho\nu\left(\frac{\partial u}{\partial y}\right)_{y=0} = \rho\left(\frac{125F^3}{216\nu x^{11}}\right)^{1/4}. \tag{7}$$

The function $f(\eta)$ in Eqs. 5–7 is determined from the solution of the ordinary differential equation $f''' + ff'' + f'^2 = 0$. The analytical solution is stated in (34). The constant F is the momentum flux of the incoming jet. For a jet impinging with a flat velocity profile, $F = (1/128)u_{\text{jet}}^3d_{\text{jet}}^4$.

Fig. 8 depicts the streamlines in the (x,y)-plane from the similarity solution for different values of the Re-number. The Re-number is a function of the maximum bubble radius only (see Eq. 4) because the diameter of the jet is fixed to 1/10th of the bubble diameter. Thus, the frames in Fig. 8 can be related to bubble radii of $R_{\max} = 50$, 100, 150, and 200 μm.

Obviously, the similarity solution loses its validity near to the stagnation point $(x, y) = (0, 0)$, e.g., the growth of the wall shear stress diverges as x approaches the origin (see Eq. 7). Thus, it becomes important to evaluate the size of the impingement region to estimate the spatial region of validity of the similarity solution.

This is done by comparing the solution of the full Navier-Stokes equation with the similarity solution. Therefore, we

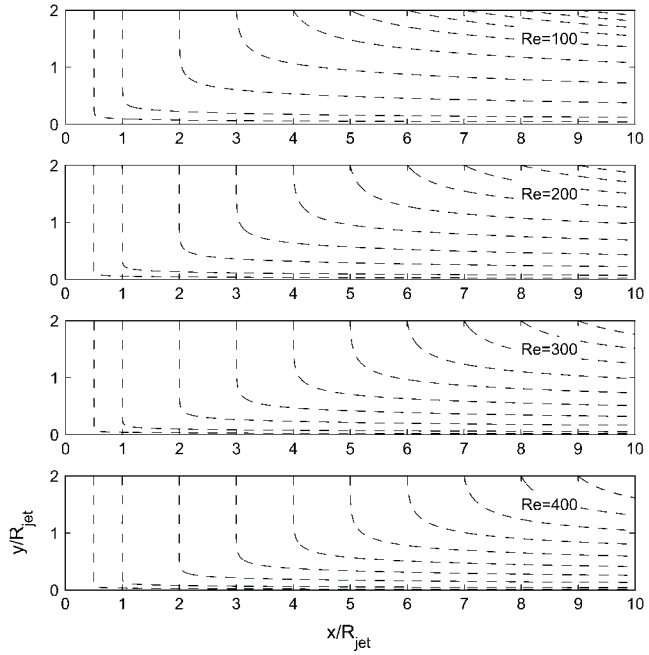

FIGURE 8 Streamlines for the similarity solution from Glauert of the wall jet for different values of the *Re*-number. The jet is flowing along the line $x = 0$ and impinging at the origin.

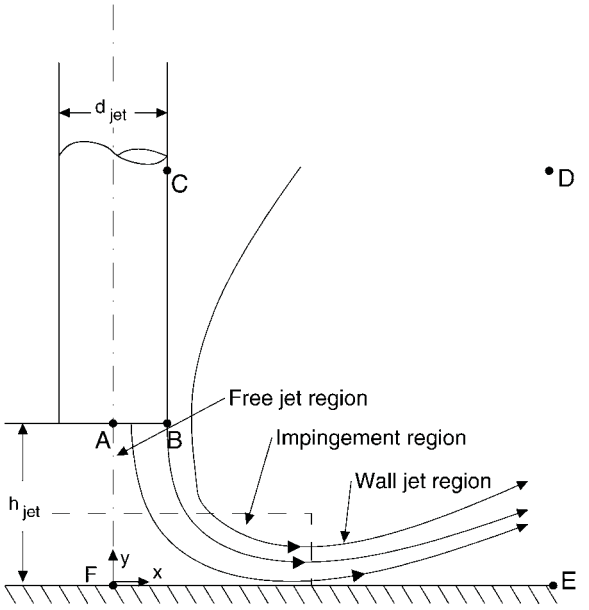

FIGURE 9 Sketch of the geometry to solve the Navier-Stokes equation in axisymmetry. The jet with a diameter of d_{jet} is released at a distance of h_{jet} from the rigid wall.

make use of a finite element solver (FEMLAB, Comsol, Los Angeles, CA) to calculate the flow field. We assume that the jet flow caused by the collapsing bubble can be modeled by a continuous discharge of a nozzle placed at a short distance from the boundary. Fig. 9 sketches the axisymmetric geometry (x,y) of the problem. The boundary conditions are defined as following: along the exit plane $\overline{\mathbf{AB}}$, free inflow with velocity $v(x, y = h) = -v_{\text{jet}}$ and $u(x, y = h) = 0$; on plane $\overline{\mathbf{BC}}$, no-slip *b.c.* $u(x = d_{\text{jet}}/2,\ y) = v(x = d_{\text{jet}}/2,\ y) = 0$; on planes $\overline{\mathbf{CD}}$ and $\overline{\mathbf{DE}}$, free outflow $p = 0$; on the rigid surface $\overline{\mathbf{EF}}$, no-slip *b.c.* $u(x, y = 0) = v(x, y = 0) = 0$; and on the axis of symmetry $\overline{\mathbf{FA}}$, symmetric *b.c.* $u(x = 0, y) = 0, \frac{\partial v}{\partial y} = 0$.

The size of the computational domain is 15-jet-diameter wide and 5-jet-diameter high. The calculations are performed for the height $h = d_{\text{jet}}/2$ of the jet from the rigid surface. The convergence test with a double refined and double widened unstructured mesh gave no noticeable deviation from the results up to the Reynolds numbers reported here. Furthermore, the good agreement with the flow pattern and values of the shear stress being reported in Deshpande and Vaishnav (35) supports our confidence that adequate convergence has been reached.

Fig. 10 depicts various streamlines; the solid square denotes the position of the incoming flow. By comparing the streamlines from the similarity solution, Fig. 8, and the full solution, Fig. 10, we find similar streamlines in the far field. In the near field there are, of course, deviations: In the full solution, the fluid entering from the top close to the pipe is sucked toward the jet and dragged under some angle to the horizontal away from the wall. This difference in the flow pattern can be attributed to the neglect of the impingement region in the similarity solution. In the impingement region, fluid is attracted toward the stagnation point leading to a region with a negative horizontal velocity, $u < 0$. This difference in flow pattern might render our approach invalid

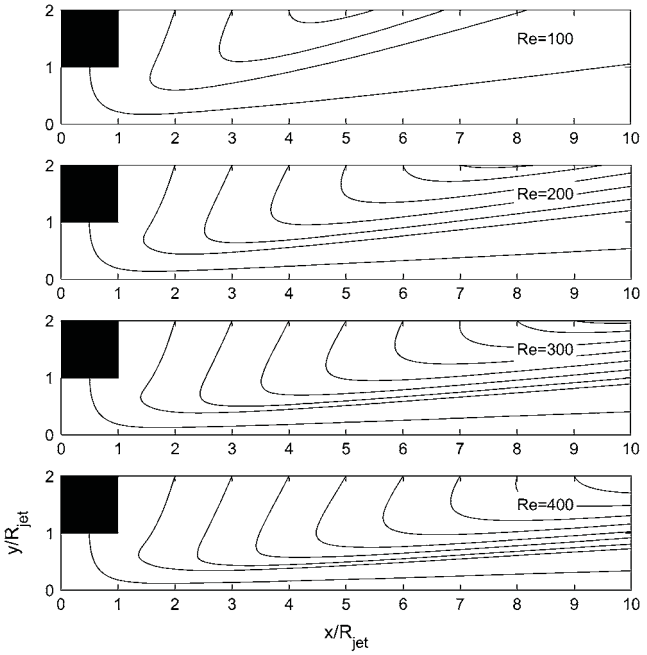

FIGURE 10 Streamlines for the full Navier-Stokes solution of the wall jet. The solid rectangle indicates the position of the incoming jet.

to adapt the similarity solution for modeling the strength of the wall shear stress (Eq. 7). To double-check, we therefore compare the magnitude of the wall shear stress from the similarity solution with the solution of the full Navier-Stokes equation.

Fig. 11 shows the horizontal velocity $u = u(x = \text{const}, y)$ for four different *Re*-numbers for various distances x/R_{jet}. The solid line depicts the flow profile from Navier-Stokes equation and the dashed line the similarity solution. The flow profile is bell-shaped, and the velocity amplitude decreases and moves upwards with distance from the stagnation point. As expected, with larger distance both solutions approach each other and a good representation of the flow profile through the similarity solution is reached. For small *Re*-numbers even around the origin $x = 0$, the agreement is good. The strongest deviations between the similarity solution and the direct numerical simulation results are obtained for $0 < x/R_{\text{jet}} < 3$ and for the largest *Re*-numbers. The wall shear stress, which is proportional to the derivative of the profile at $y = 0$ of Fig. 11, is overestimated by the similarity solution in that range.

The wall shear stress as a function of the distance is plotted in Fig. 12 for the same range of *Re*-numbers. Note the logarithmic scale on the *y* axis. The solution of the Navier-Stokes equation (*solid line*) increases from zero at the stagnation point, reaches a maximum at $x/R_{\text{jet}} \approx 1.5$ and drops again for larger distances. In contrast, the similarity solution (*dashed line* in Fig. 12) starts from infinity (see Eq. 7) and approaches the Navier-Stokes solution with increasing x/R_{jet} asymptotically. From Fig. 12, it becomes evident that the similarity solution allows for a very reasonable estimate of the wall shear for normalized distances already from $x/R_{\text{jet}} > 3$ on.

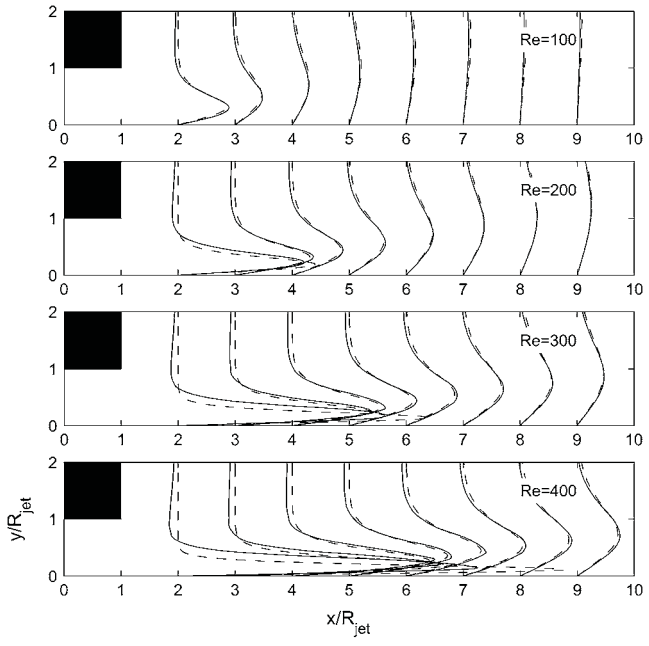

FIGURE 11 Profiles of the horizontal flow velocity for the full solution (*solid lines*) and the self-similar solution (*dashed lines*). For larger distances R_{jet} from the origin, both models show good agreement.

Model for the detachment dynamics

Adherent cells on the substrate being exposed to a sufficient wall shear stress become detached and are transported with the flow. For an estimate of the size of the depleted area the process of bond breaking between the cell membrane and the substrate has to be evaluated. Here, we make use of a peeling model for cell detachment derived by Garrivier et al. (36). The process of detachment is described by a fracture process of the bonds in the adhesive belt. Their model has been validated experimentally in a planar shear-flow setup.

Let us rewrite the main model equations: The detachment efficiency *n* after time *t*, i.e., the percentage of detached cells, is given by the rate equation

$$n = 1 - \exp(-k(\tau)t), \tag{8}$$

where $k(\tau)$ is the shear-stress dependent detachment rate defined through Eq. 9. The detachment rate constant $k(\tau)$ is therefore the inverse of the typical time needed to detach a cell exposed to hydrodynamic shear stress τ. It is expressed as (36)

$$k(\tau) = k_0 \frac{\exp(\sqrt{\tau/4\tau_0})}{(\tau/4\tau_0)^{1/4}}, \tag{9}$$

where k_0 and τ_0 are parameters of the cell type and substrate. These two constants are estimated with values for *Dictyostelium discoideum* on a glass substrate taken from Décavé et al. (37) with $k_0 = 2 \times 10^{-4}\ \text{s}^{-1}$ and $\tau_0 = 0.08$ Pa.

The critical shear stress τ_c to cause cell detachment can be obtained by solving Eqs 8 and 9 for τ. The time *t* in Eq. 8 is the duration the shear stress lasts and can be identified with the collapse time T_C (see Eq. 1). For convenience, we identify full detachment with $n = n_f = 99\%$. The shear stress as a function of the distance from the stagnation point is given as a monotonic function. Therefore, the critical shear stress τ_c can be identified uniquely with the radius of detachment.

By considering the diameter of the jet as a function of the bubble diameter and using the estimate for the constant jet velocity from Eq. 2, we can numerically solve for the radius of the detachment area, x_c, as a function of the bubble radius.

Yet, an approximation of the critical shear stress can be obtained analytically by inserting Eq. 9 into the rate Eq. 8, solving for τ_c, and neglecting terms of the order $\log(\tau/\tau_0)$. This is justified for large wall shear stresses when $\tau_c/\tau_0 \gg \log(\tau_c/\tau_0)$. The critical shear stress is thus approximated by

$$\tau_c \approx 4\tau_0 \left[\log\left(\frac{-\log(1-n_f)}{4k_0 T_C}\right)\right]^2, \tag{10}$$

with T_C given by Eq. 1. Fig. 13 illustrates the radius of the cell-depleted area, x_c versus the maximum bubble radius. The radius of the depleted area increases with increasing

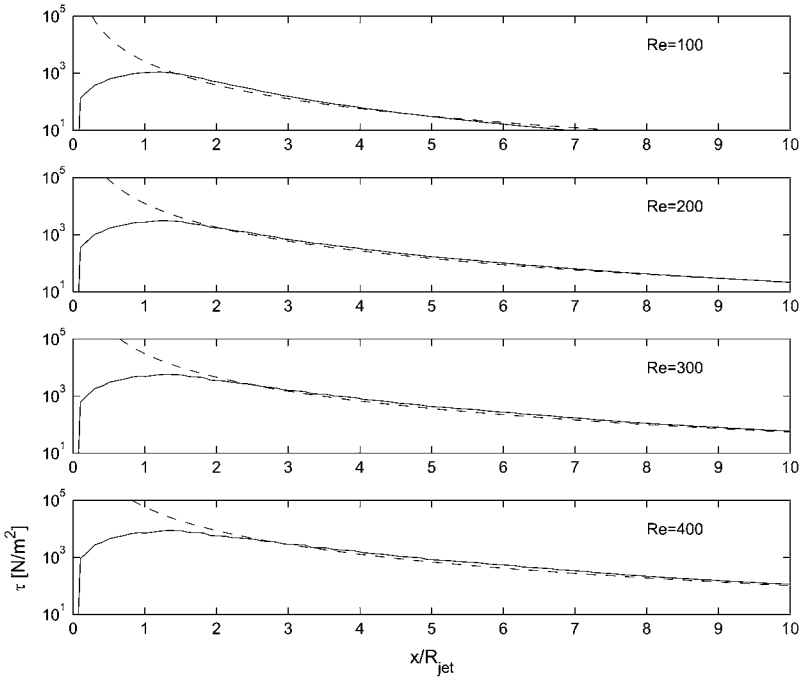

FIGURE 12 The wall shear stress as a function of the distance for the full solution (*solid lines*) and the self-similar Glauert solution. For distances larger than ~3 R_{jet} from the origin, good agreement is obtained.

bubble radius. Here, the solid curve depicts the numerical solution and the (hardly distinguishable) dashed curve depicts the solution using the approximation from Eq. 10. In any case, bubbles in the range of 0.1–1 mm cause a depletion area of 1.6–1.8 times their maximum bubble size.

Comparison experiment with theory

Now let us compare the predicted size of the detached area from Fig. 13 for the measured maximum bubble radius of 0.8 mm: Fig. 13 suggests an detachment radius of 1.36 mm, which should correspond to the asymptotic value in Fig. 7 of 0.95 mm. Although there is a discrepancy of 40%, we consider this as a reasonable estimate while keeping in mind the coarse simplifications introduced in the model. Two additional measurements from other runs of the high-speed photography are depicted in Fig. 13 as solid squares. Still, more measurements are necessary to strengthen the observation, that smaller bubbles cause smaller areas of detachment. Yet, the obtained data supports the trend of the model.

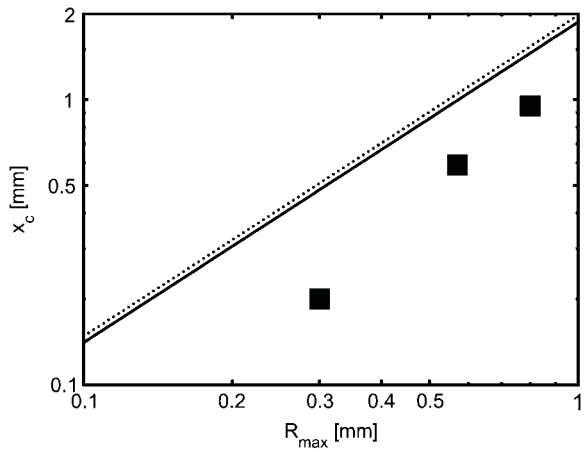

FIGURE 13 Radius of the detachment area x_c as a function of the maximum bubble radius R_{max} obtained from the numerical solution of Eq. 8 for τ_c (*solid line*) and through the approximation Eq. 10 (*dotted line*). The solid squares denote measurements.

We mention that, when cavitation nuclei (ultrasound contrast agent Levovist from Schering, Berlin, Germany mixed at a concentration of 10 mg/ml) are added, many more bubbles are nucleated. These, however, grow much less—presumably due to the bubble-bubble interaction. Instead of circular sites of detachment reported in this publication, we find scattered sides of drug delivery with a few cells involved and no detached cells.

SUMMARY

In summary, we demonstrate that cavitation bubbles and not the shock wave itself is causing drug delivery for the experimental conditions reported here. High-speed images capture cells transported with a radial flow, which we explain with a radial spreading flow. It is formed during the aspherical collapse leading to a wall jet flow. The resulting boundary layer flow makes the cells experience a strong shear, which finally causes cell detachment. Cells lining the border of the detached area are showing permanent poration due to large lesions in the cell membrane. Cells further away show repairable poration and uptake of a non-membrane-permeant dye (calcein).

APPENDIX: COMMENT ON THE FLOW FIELD OF COLLAPSING BUBBLES NEAR BOUNDARIES

In this Appendix we discuss in more detail the simplifying assumption of a radial spreading wall jet: The jet flow from bubbles collapsing near boundaries impacts on the boundary before the bubble has reached its minimum size. Because of that the outwards spreading wall jet flow eventually collides with the radially inwards directed flow due to the still shrinking bubble leading to liquid acceleration away from the wall (depicted, for example, in Fig. 5 of (38)). This phenomenon has been termed ''splash'' by Tong et al. (39). The splashing of liquid has been found for nondimensionalized standoff distances, $\gamma = s/R_{max}$, between 0.6 and 1.2, where s is the initial distance between the bubble center and the boundary. High-speed photography (38–40) depicts the deformation of the bubble shape during the splash. At later stage, the splash induces a toroidal vortex at the wall.

Potential flow calculations, e.g., those of Pearson et al. (41), are in excellent agreement with experimental observations. Therefore, one wonders if a simple wall jet flow is able to model the essential flow field close to the boundary. Here, we argue that although liquid from the wall jet is accelerated away from the boundary, the relevant fluid dynamics for the cell detachment takes place in the boundary layer, which cannot be captured within the potential flow framework and which was not studied in the above cited experiments.

To obtain more insight on the competition between the outward spreading flow (the wall jet) and the inward one (the sink flow), we compare their magnitude for a typical case. The maximum velocity of the wall jet flow, u_{out}, can be readily calculated with Eq. 5 and the knowledge that the maximum of the function $df(\eta)/d\eta$, which is 0.32 (34). In contrast, a typical radial inward velocity caused by the shrinking bubble is approximated with a sink located at a distance l from a rigid boundary. From potential flow theory, the inward velocity u_{in} can be calculated with

$$u_{in} = \frac{2R^2\dot{R}x}{(l^2 + x^2)^{3/2}}, \tag{11}$$

where R is the bubble radius and $\dot{R}$ is the bubble wall velocity. We further estimate an upper bound of u_{in} by setting $l = 0$ in Eq. 11. We find that the velocity $u_{in}(x)$ for a typical case (see (38), Figs. 3 and 4, with $\gamma = 1.1$, $R_{max} =$ 1.4 mm, $\dot{R} =$ 35 m/s, and $u_{jet} =$ 60 m/s) is at least an order-of-magnitude smaller than $u_{out}(x)$. Thus we argue that the boundary layer flow caused by the jet is only weakly modified by the splashing phenomena. We also stress that the splash lasts only for a few microseconds; see, e.g., the reversal of the near-boundary velocity vectors in Fig. 5, *b* and *c*, of Brujan et al. (38). Shortly after, the wall jet and the toroidal vortex flow induced by the splash are oriented in the same direction.

Our argument of the importance of the wall jet is in full agreement with the observation in our Fig. 6. Here, no cell removal is found during the collapse of the bubble, thus the velocity gradients induced by the inward flow are too weak. In contrast, the outwards-directed jet flow causes immediate detachment.

We are very thankful to Yvonne Kraan from the cell lab for her help with the cell cultivation work. Further, we thank Gert-Wim Bruggert for construction of various apparatus.

This work is financially supported through Stichting voor Fundamenteel Onderzoek der Materie (FOM, The Netherlands), under grant No. 00PMT04. C.D.O. acknowledges the support from the Nederlandse Organisatie voor Wetenschappelijk Onderzoek (NWO, The Netherlands) through the VIDI grant.

REFERENCES

1. Miller, M. W., D. L. Miller, and A. A. Brayman. 1996. A review of in vitro bioeffects of inertial ultrasonic cavitation from a mechanistic perspective. *Ultrasound Med. Biol.* 22:1131–1154.
2. Ng, K., and Y. Liu. 2002. Therapeutic ultrasound: its application in drug delivery. *Med. Res. Rev.* 22:204–223.
3. Bao, S. P., B. D. Thrall, and D. L. Miller. 1997. Transfection of a reporter plasmid into cultured cells by sonoporation in vitro. *Ultrasound Med. Biol.* 23:953–959.
4. Ward, M., J. R. Wu, and J. F. Chiu. 1999. Ultrasound-induced cell lysis and sonoporation enhanced by contrast agents. *J. Acoust. Soc. Am.* 105: 2951–2957.
5. Stride, E., and N. Saffari. 2003. Microbubble ultrasound contrast agents: a review. *Proc. Instn. Mech. Engrs.* 217:429–447.
6. Lee, S., T. Anderson, H. Zhang, T. J. Flotte, and A. G. Doukas. 1996. Alteration of cell membrane by stress waves in vitro. *Ultrasound Med. Biol.* 22:1285–1293.
7. Lokhandwalla, M., and B. Sturtevant. 2001. Mechanical haemolysis in shock wave lithotripsy (SWL). I. Analysis of cell deformation due to SWL flow-fields. *Phys. Med. Biol.* 46:413–437.
8. Sundaram, J., B. R. Mellein, and S. Mitragotri. 2003. An experimental and theoretical analysis of ultrasound-induced permeabilization of cell membranes. *Biophys. J.* 84:3087–3101.
9. Lokhandwalla, M., J. A. McAteer, J. C. Williams, Jr., and B. Sturtevant. 2001. Mechanical haemolysis in shock wave lithotripsy (SWL). II. In vitro cell lysis due to shear. *Phys. Med. Biol.* 46:1245–1264.
10. Wu, J., J. P. Ross, and J. F. Chiu. 2002. Reparable sonoporation generated by microstreaming. *J. Acoust. Soc. Am.* 111:1460–1464.
11. Ohl, C. D., and B. Wolfrum. 2003. Detachment and sonoporation of adherent HeLa-cells by shock wave-induced cavitation. *Biochim. Biophys. Acta Gen. Subj.* 1624:131–138.
12. Wolfrum, B., R. Mettin, T. Kurz, and W. Lauterborn. 2002. Observations of pressure-wave-excited contrast agent bubbles in the vicinity of cells. *Appl. Phys. Lett.* 81:5060–5062.
13. Lauer, U., E. Burgelt, Z. Squire, K. Messmer, P. H. Hofschneider, M. Gregor, and M. Delius. 1997. Shock wave permeabilization as a new gene transfer method. *Gene Ther.* 4:710–715.
14. Crum, L. A., and G. M. Hansen. 1984. Generalized equations for rectified diffusion. *J. Acoust. Soc. Am.* 72:1586–1592.
15. Fyrillas, M. M., and A. J. Szeri. 1994. Dissolution and growth of soluble spherical oscillating bubbles. *J. Fluid Mech.* 277:381–407.
16. Hilgenfeldt, S., D. Lohse, and M. Brenner. 1996. Phase diagram for sonoluminescing bubbles. *Phys. Fluids.* 8:2808–2826.
17. Brenner, M., S. Hilgenfeldt, and D. Lohse. 2002. Single bubble sonoluminescence. *Rev. Mod. Phys.* 74:425–484.
18. Sondén, A., B. Svenson, N. Roman, H. Östmark, B. Brismar, J. Palmblad, and B. T. Kjellström. 2000. Laser-induced shock wave endothelial cell injury. *Lasers Surg. Med.* 26:364–375.
19. Kodama, T., M. R. Hamblin, and A. G. Doukas. 2000. Cytoplasmic molecular delivery with shock waves: importance of impulse. *Biophys. J.* 79:1821–1832.
20. Rau, K. R., A. Guerra, A. Vogel, and V. Venugopalan. 2004. Investigation of laser-induced cell lysis using time-resolved imaging. *Appl. Phys. Lett.* 84:2940–2942.
21. Chin, C. T., C. Lancée, J. Borsboom, F. Mastik, M. E. Frijink, N. de Jong, M. Versluis, and D. Lohse. 2003. Brandaris 128: a digital 25 million frames per second camera with 128 highly sensitive frames. *Rev. Sci. Instr.* 74:5026–5034.
22. Ting-Beall, H. P., D. V. Zhelev, and R. M. Hochmuth. 1995. Comparison of different drying procedures for scanning electron microscopy using human leukocytes. *Microsc. Res. Tech.* 32:257–361.
23. Junge, L., C. D. Ohl, B. Wolfrum, M. Arora, and R. Ikink. 2003. Cell detachment method using shock-wave-induced cavitation. *Ultrasound Med. Biol.* 29:1769–1776.
24. Arora, M., L. Junge, and C. D. Ohl. 2005. Cavitation cluster dynamics in shock-wave lithotripsy. 1. Free field. *Ultrasound Med. Biol.* 31: 827–839.
25. Leighton, T. G. 1994. The Acoustic Bubble. Academic Press, London.
26. Kudo, N., T. Miyaoka, K. Okada, and K. Yamaoto. 2002. Study on mechanism of cell damage caused by microbubbles exposed to ultrasound. *IEEE Ultrasonics Symp. Proc.* 2:1383–1386.

27. Vogel, A., W. Lauterborn, and R. Timm. 1989. Optical and acoustic investigations of the dynamics of laser-produced cavitation bubbles near a solid boundary. *J. Fluid Mech.* 106:199–338.

28. Best, J. P., and J. R. Blake. 1994. An estimate of the Kelvin impulse of a transient cavity. *J. Fluid Mech.* 261:75–93.

29. Vogel, A., P. Schweiger, A. Frieser, M. N. Asiyo, and R. Birngruber. 1990. Intraocular Nd:YAG laser surgery: light-tissue interaction, damage range, and reduction of collateral effects. *IEEE J. Quantum Electron.* 26:2240–2260.

30. Lauterborn, W., and H. Bolle. 1975. Experimental investigations of cavitation-bubble collapse in the neighborhood of a solid boundary. *J. Fluid Mech.* 72:391–399.

31. Blake, J. R., G. S. Keen, R. P. Tong, and M. Wilson. 1999. Acoustic cavitation: the fluid dynamics of non-spherical bubbles. *Philos. Trans. R. Soc. Lond. A.* 357:251–267.

32. Philipp, A., and W. Lauterborn. 1998. Cavitation erosion by single laser-produced bubbles. *J. Fluid Mech.* 361:75–116.

33. Kodama, T., and K. Takayama. 1998. Dynamic behavior of bubbles during extracorporeal shock-wave lithotripsy. *Ultrasound Med. Biol.* 24:723–738.

34. Glauert, M. B. 1956. The wall jet. *J. Fluid Mech.* 1:625–643.

35. Deshpande, M. D., and R. N. Vaishnav. 1982. Submerged laminar jet impingement on a plane. *J. Fluid Mech.* 114:213–236.

36. Garrivier, D., E. Décavé, Y. Bréchet, F. Bruckert, and B. Fourcade. 2002. Peeling model for cell detachment. *Eur. Phys. J. E.* 8:79–97.

37. Décavé, E., D. Garrivier, Y. Bréchet, B. Fourcade, and F. Bruckert. 2002. Shear flow-induced detachment kinetics of *Dictyostelium discoideum* cells from solid substrate. *Biophys. J.* 82:2383–2395.

38. Brujan, E. A., G. S. Keen, A. Vogel, and J. R. Blake. 2002. The final stage of the collapse of a cavitation bubble close to a rigid boundary. *Phys. Fluids.* 14:85–92.

39. Tong, R. P., W. P. Schiffers, S. J. Shaw, J. R. Blake, and D. C. Emmony. 1999. The role of ''splashing'' in the collapse of a laser-generated cavity near a rigid wall. *J. Fluid Mech.* 380:339–361.

40. Lindau, O., and W. Lauterborn. 2003. Cinematographic observation of the collapse and rebound of a laser-produced cavitation bubble near a wall. *J. Fluid Mech.* 479:327–348.

41. Pearson, A., J. R. Blake, and S. R. Otto. 2004. Jets in bubbles. *J. Eng. Math.* 48:391–412.